Thermal study of clogging during filament-based material extrusion additive manufacturing: Experimental-numerical study

Zahra Taheri[a] , Ali Karimnejad Esfahani[b] , Abas Ramiar[a,*]

[a]Faculty of Mechanical Engineering, Babol Noshirvani University of Technology, Babol, Iran

[b]Department of Mechanical Engineering, Ferdowsi University of Mashhad, Mashhad, Iran

Abstract

One of the major drawbacks of material extrusion additive manufacturing (AM) is hot-end clogging. This study aims to answer the question, “What thermal conditions lead to clogging during filament-based material extrusion?” Answering this question requires a clear understanding of temperature distribution inside the liquefier. However, this could not be achieved only through experimental measurements. Therefore, numerical simulations were also carried out by developing a 3D finite volume model of the hot-end. The results obtained from numerical simulations show good agreement with experimental measurements. They also give us a detailed picture of the temperature gradient near the nozzle. Moreover, a series of experiments were performed to determine when clogging occurs, and some criteria for avoiding clogging were presented. These results were also compared and combined with the numerical results to investigate the thermal condition leading to clogging. As the results show, overheating the heat

* Corresponding author: Associate professor, Faculty of Mechanical Engineering, Microfluidics and MEMS lab, Babol Noshirvani University of Technology Tel/Fax: +981132334205, Email: aramiar@nit.ac.ir

barrier increases the length of the filament, whose temperature is above the glass transition temperature. As this length exceeds a critical value, the filament buckles under the extruder motor force and clogging occurs.
Keywords: Clogging, Multi-material printing, Material extrusion, Numerical simulation, Heat transfer, buckling

1. Introduction

The global additive manufacturing (AM) market size has been growing steadily and is expected to reach USD 34.8 billion by 2024 [1]. During the AM process, the part is built layer by layer based on a computer-aided design (CAD) model. There are seven major branches of 3D printing techniques: Vat photopolymerization, material jetting, binder jetting, powder bed fusion, material extrusion, directed energy deposition, and sheet lamination [2]. Among them, material extrusion (also known as fused filament fabrication, FFF) is the most common method because its process is simple and incurs lesser manufacturing cost.

The filament-based material extrusion technique has made its way into a wide range of applications like rapid prototyping [3], art [4,5], and medical fields [6-8]. It is also widely used to make metamaterials that have broad potential applications [9].

Despite the wide range of applications of this technique, there are still some defects and process failures to overcome, like hot-end clogging, overflow, layer separation, and warping. Among them, hot-end clogging is one of the most significant process failures. To detect clogging, some researchers compared the printing part with the original CAD model during the printing process using various tools, such as image processing software [10], visible

light 3D scanning systems [11], and augmented reality (AR) toolkit [12]. Some others presented a physics-based dynamic model of the process and identified the process errors using vibration signals gathered from vibration sensors [13,14]. The studies mentioned above have focused on detecting and monitoring clogging during the printing process. However, potential factors causing nozzle clogging must be identified to avoid this process failure. One of these factors is incorporating high loadings of nanomaterials [15] or using reinforced polymers at higher filler contents [16]. Beran et al. [16] investigated potential factors that can cause nozzle clogging for a filled polymer, such as nozzle and filler diameters, resin viscosity, and filler volume fraction.

Other factors can also lead to clogging, such as dust or burnt filament inside the liquefier, insufficient layer height, warping of the printing part [13], and inappropriate liquefier cooling. Among these factors, inappropriate liquefier cooling is one of the most common reasons for clogging since nearly half of all E3D-v6 hot-end issues are related to inadequate liquefier cooling conditions [17]. On the other hand, overcooling can lead to energy waste because more energy is needed to keep the nozzle temperature at the desired value and drive the fan at higher speeds for higher air delivery rates. So, it seems that the liquefier's thermal behavior plays a vital role in clogging and needs to be investigated.

Jerez-Mesa et al. [18] studied the thermal behavior of the BCNozzle, designed at the BCN3D Technologies, and presented a relationship between fan air velocity and heat sink temperature. In another study [19], the thermal performance of 3 different heat sinks, including BCNozzle, were compared with each other to determine the most efficient design. Despite these limited thermal studies on hot-ends, to the knowledge of the authors, no study has

addressed the thermal conditions that lead to clogging, as is the aim of this paper.

Considering growing multicolor printing applications [20-22], the RepRap multi-material Diamond hot-end has been selected for investigation in this study. This nozzle has also been shown to have many advantages, including efficient fabrication of gradient materials, easy calibration, and better precision [23] [24].

This study aims to give a precise and practical insight into the clogging phenomenon in filament-based material extrusion technique. Two different materials of ABS and PLA are considered in this study because of their widespread use. To investigate the thermal conditions leading to clogging, in the beginning, the temperature distribution along the heat sink has been investigated experimentally and numerically at various fan airflow velocities. The results show considering the radiation heat transfer is vital to achieve a good agreement between numerical and experimental results, especially at low fan airflow velocities. In this paper, the effects of considering the radiation model in numerical simulations are discussed at zero and non-zero fan airflow velocities, and the minimum airflow velocity at which radiation heat transfer can be safely neglected is determined. Based on the results obtained from numerical simulations and the experiments designed and performed to detect clogging, a good insight into the clogging mechanism is achieved. The results show that in poor cooling conditions, the length of the filament inside the heat barrier, whose temperature is above the glass transition temperature, increases considerably, and under the extruder motor force, it buckles and consequently clogs the hot-end.

2. Experimental set-up

According to Fig. 1, the RepRap Diamond hot-end consists of 4 main components: a Diamond nozzle, a cooler shield, three E3D-Lite6 heat sinks including a heat barrier inside each of them, and a $50mm$ fan. A $40W$ cartridge heater heats the Diamond nozzle. It is maintained at the desired temperature by a control loop and a $100k\Omega$ NTC thermistor that measures the nozzle temperature. Fig. 2 shows the RepRap Diamond nozzle in detail.

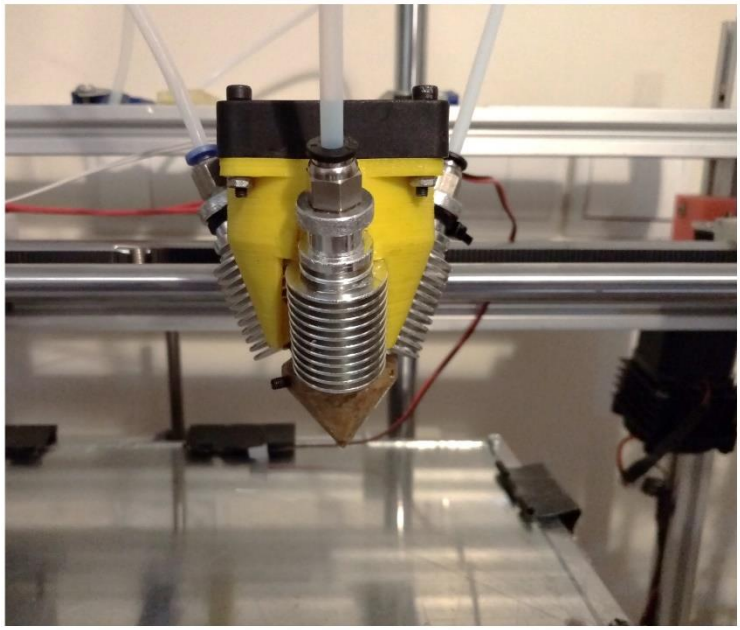

Fig. 1 RepRap Diamond hot-end used in this study

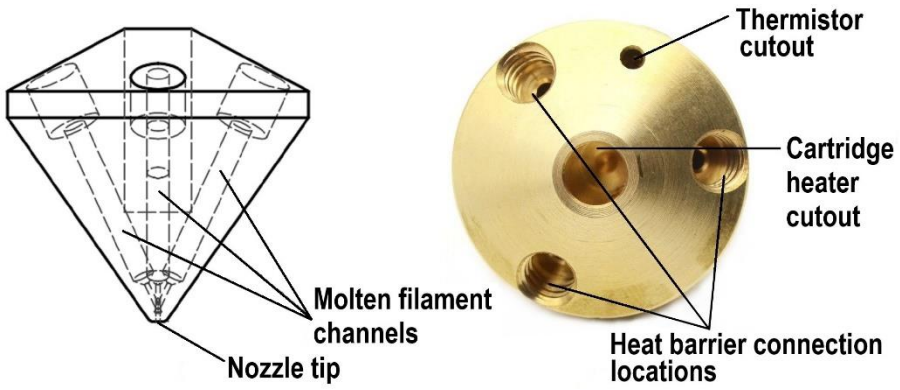

Fig. 2 RepRap Diamond nozzle

A core x-y filament-based material extrusion printer built by the authors was used to study the thermal performance and the clogging phenomenon in the Diamond hot-end. Open-source Marlin firmware was uploaded to the MKS GEN V1.4 board. Four $100k\Omega$ NTC thermistors were attached to the heat sink by Kapton tape to record the temperature along it. Fig. 3 shows the configuration of the hot-end in the experiments. The more precise locations of the thermistors are illustrated in Fig. 4. The Repetier-Host V2.1.5 was selected as the machine control software to control the nozzle temperature, airflow velocity, and other printing parameters.

For cooling, a FONSONING FSY50S12H fan was used and connected to the fan terminal on the board. It was done only to facilitate the control of the fan input voltage under the manual control tab in Repetier-Host. It should be noted that in the actual printing process, the heat sink cooling fan should not be connected to this terminal. Because it is dedicated to another fan that is used for cooling the freshly deposited material, especially in overhangs, bridges, and small details to provide a suitable base for the next layer [25]. Incorrect use of this terminal for heat sink cooling fan is one of the common causes of clogging in the actual printing process [17].

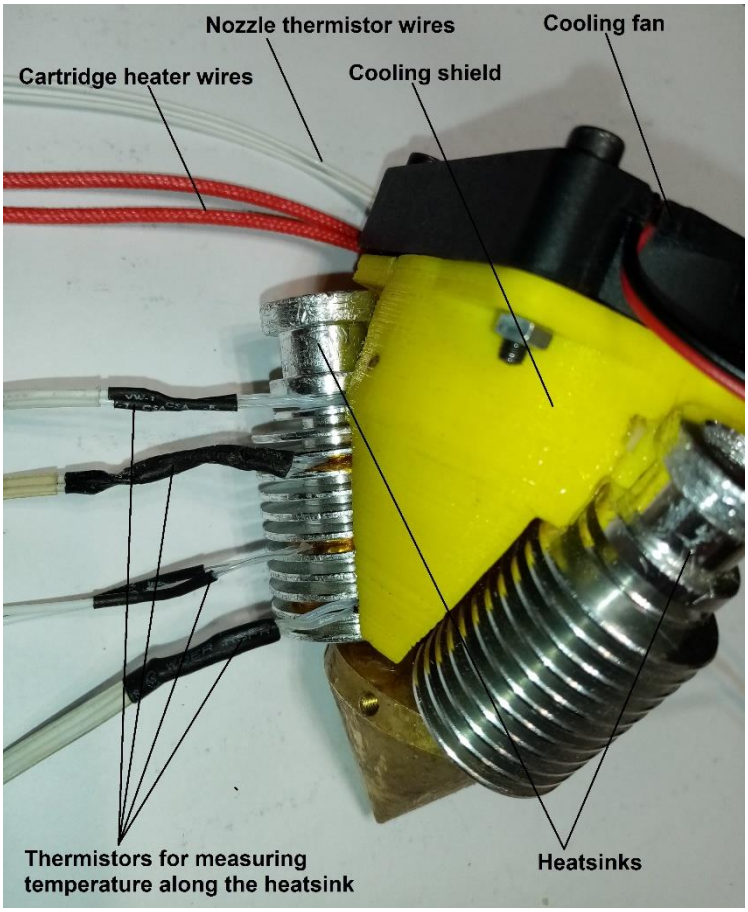

Fig. 3 The configuration of the hot-end for experiments in this study

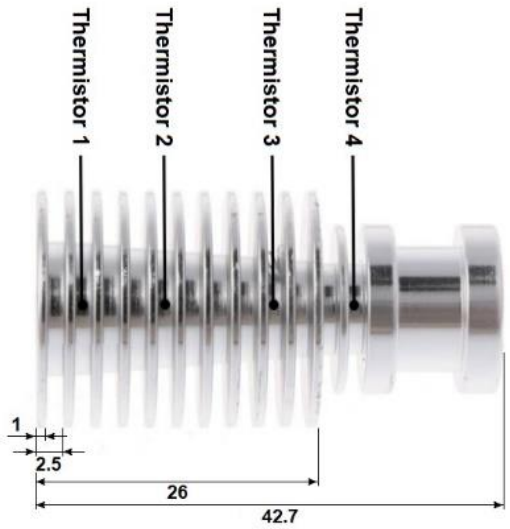

Fig. 4 The position of thermistors on the heat sink

Fan velocity was controlled by adjusting the voltage applied to the fan. Percentage values of 15%, 20%, 30%, 40%, 50%, and 60% of board input voltage were applied using Repetier manual control tab to produce different voltages and airflow rates. The board input voltage was $12V$. It should be noted that higher voltage percentages were avoided since further increasing the airflow velocity had little effect on the temperature distribution along the heat sink. This is mostly due to the dominance of forced convection that will be discussed later.

The experimental procedure to study the temperature distribution along the heat sink was as follows:

- At the beginning of each test, the fan was turned on at the desired percentage of the input voltage.
- The ambient temperature was approximately $27^{\circ}C$, and the nozzle was heated to $210^{\circ}C$ for the PLA, and $260^{\circ}C$ for the ABS.
- The heat sink was left for at least 30 minutes to reach a stable thermal condition.
- Under stable conditions, temperature values obtained from the thermistors were recorded.

Experiments repeated at least four times for all voltages and nozzle temperatures. Finally, the average of the results was calculated and reported.

A cube with dimensions of 15mm×15mm×20mm was printed to investigate the impact of heat sink cooling conditions on the clogging phenomenon during the printing process. The process parameters are shown in Table 1.

Table 1 Process parameters for clogging experiments for both PLA and ABS printing processes

Layer Height	0.3mm	Number of top solid layer	2
First layer height	0.32mm	Number of bottom solid layer	2
Fill density	90%	Number of perimeters	2
Fill pattern	Concentric	Extrusion width	0.4mm
Print speed	10mm/s	Nozzle temperature for PLA**	$210^{\circ}C$
Retract speed	30mm/s	Nozzle temperature for ABS**	$260^{\circ}C$
Retraction length	3mm*		

* Appropriate length for a Bowden extruder [26].

**Made in Shenzhen Yongchanghe Technology CO., LTD.

The clogging test steps were as follows:

- The ambient temperature was approximately $27^{\circ}C$. The first five layers were printed at maximum fan speed to ensure that other potential factors such as the presence of burnt filament and dust did not cause clogging.
- After the first five layers, the fan voltage was adjusted to the desired value for that test.
- The printing process was monitored precisely. There were three different scenarios: (1) Complete clogging, (2) no complete clogging but with some problems, and (3) the printing process without any problem. If clogging was identified, the operation was stopped, and the hot-end was cleaned for the next experiment.

These experiments were also repeated four times for all fan voltages.

3. Numerical simulation

As shown in Fig. 5, a 3D model was developed to analyze the Diamond hot-end numerically. The hot-end geometry shows a rotational periodicity of 120

deg, bringing about a significant reduction of modeled volume and calculation costs. The model consists of six different domains: A Diamond nozzle made of brass, a heat barrier made of stainless steel, an E3D-Lite6 heat sink made of aluminum, a Diamond cooler shield printed with ABS filament, a feedstock filament of ABS or PLA, and an air domain.

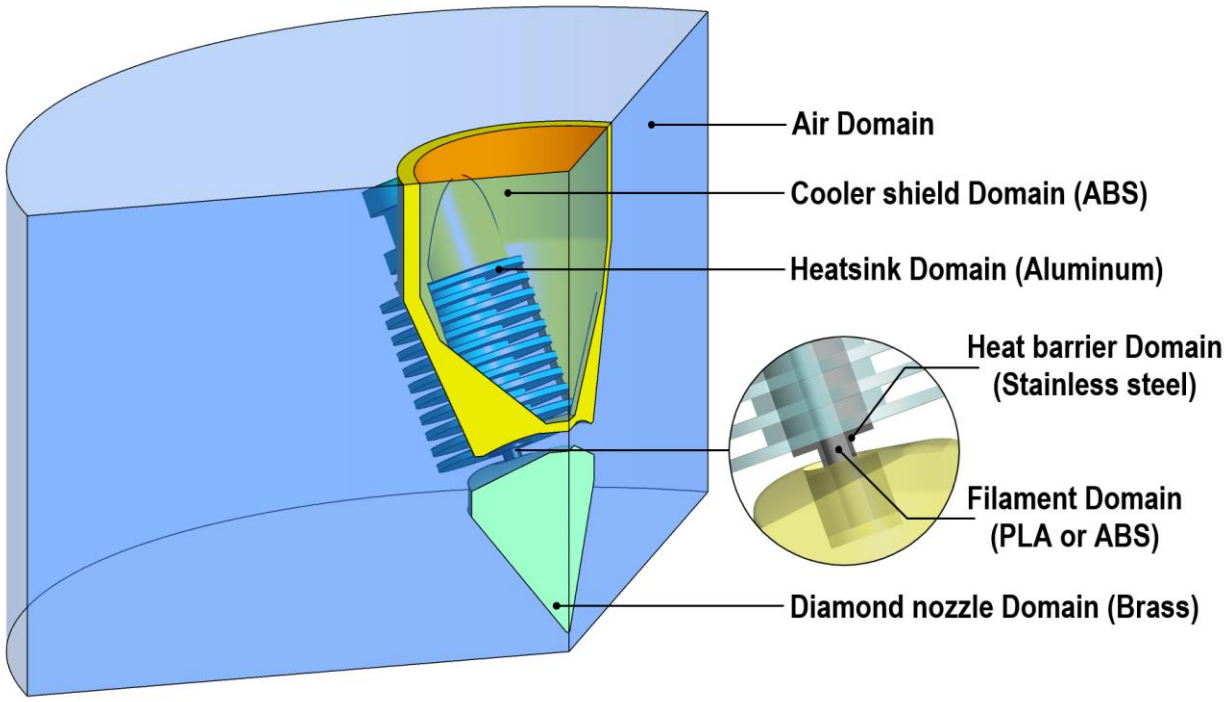

Fig. 5 3D model of the Diamond hot-end used for numerical simulations

3.1. Governing equations

Numerical simulation of Diamond hot-end heat transfer was performed by considering conduction, convection, and radiation heat transfer. The continuity (Eq. 1) and Navier-Stocks (Eq. 2) equations were solved for the fluid region, while the energy equation (Eq. 3) was solved for both fluid and solid regions. Taking into account that our analysis was performed in the steady-state condition, and there was no mass or heat generation, the equations can be presented as below:

$$\nabla.(\rho\vec{v}) = 0 \qquad (1)$$

Where ρ is the fluid density and $\vec{v}$ is the fluid velocity.

$$\rho(\vec{v}.\nabla\vec{v}) = -\nabla p + \nabla.\left(\mu(\nabla\vec{v} + (\nabla\vec{v})^T) - \frac{2}{3}\mu(\nabla.\vec{v})I\right) + \rho\vec{g} \quad (2)$$

Where p is the fluid pressure, μ is the fluid dynamic viscosity, I is the unit tensor, and $\rho\vec{g}$ is the gravitational force.

$$\rho C_p\vec{v}.\nabla T = \nabla.(k\nabla T) \quad (3)$$

Where C_p is the thermal capacity, k is the thermal conductivity, and T is the temperature. Note that, as the Brinkman number is quite small, energy transfer through viscous dissipation was neglected.

The k-ε turbulence model was used to capture any turbulence in the airflow field. This model yields good accuracy in the absence of large adverse pressure gradients [27] while it uses just two additional transport equations, one for the turbulent kinetic energy (k) (Eq. 4) and one for the dissipation rate of turbulent kinetic energy (ε) (Eq. 5). Therefore, computational costs are not drastically affected.

$$\frac{\partial}{\partial t}(\rho k) + \frac{\partial}{\partial x_i}(\rho k u_i) = \frac{\partial}{\partial x_j}\left[\left(\mu + \frac{\mu_t}{\sigma_k}\right)\frac{\partial k}{\partial x_j}\right] + G_k + G_b - \rho\varepsilon \quad (4)$$

$$\frac{\partial}{\partial t}(\rho\varepsilon) + \frac{\partial}{\partial x_i}(\rho\varepsilon u_i) = \frac{\partial}{\partial x_j}\left[\left(\mu + \frac{\mu_t}{\sigma_\varepsilon}\right)\frac{\partial\varepsilon}{\partial x_j}\right] + C_{1\varepsilon}\frac{\varepsilon}{k}(G_k + C_{3e}G_b) - C_{2\varepsilon}\rho\frac{\varepsilon^2}{k} \quad (5)$$

$C_{1\varepsilon}$, $C_{2\varepsilon}$, C_μ, σ_k, and σ_ε are model constants whose values are as follows [28]: $C_{1\varepsilon} = 1.44$, $C_{2\varepsilon} = 1.92$, $C_\mu = 0.09$, $\sigma_k = 1.0$ and $\sigma_\varepsilon = 1.3$.

Also G_k and G_b are the generation of turbulent kinetic energy due to mean velocity gradients and buoyancy, respectively, and μ_t represents turbulent viscosity.

In this study, the Discrete Ordinate (DO) model was used to model the radiation effects. As a beam of radiation travels through a medium, it may lose energy because of medium absorption, gain energy from medium emissions, or its energy may be increased or decreased by medium

scattering. The differential form of radiative transfer equation (RTE) for a beam in the direction $\vec{s}$ and position $\vec{r}$ can be written as:

$$\frac{dI(\vec{r}.\vec{s}')}{ds} + (a + \sigma_s)I(\vec{r}.\vec{s}') = an^2\frac{\sigma T^4}{\pi} + \frac{\sigma_s}{4\pi}\int_0^{4\pi} I(\vec{r}.\vec{s}')\phi(\vec{s}.\vec{s}')d\Omega' \qquad (6)$$

Where $\vec{r}$ is the position vector, $\vec{s}$ is the direction vector, $\vec{s}'$ is the scattering directional vector, s is the path length, a is the absorption coefficient, n is the reflective index, σ_s is the scattering coefficient, ϕ is the phase function, Ω' is the solid angle, and I is the radiation intensity. σ is the Stefan-Boltzmann constant and equal to $5.67 \times 10^{-8}\ W/m^2K^4$.

DO transforms RTE into a set of simultaneous partial differential equations. In the DO model, the equation of RTE (Eq. 6) is solved for a set of discrete directions that covers total angular space 4π sr. So that each octant of angular space was discretized to 4 polar angles (N_θ) and 4 azimuthal angles ($N_\emptyset$), which means $8 \times 4 \times 4$ solid angles. All solid angles were divided into 3×3 pixels. All surfaces were assumed to be opaque, diffuse, and gray.

3-2 Boundary conditions

As previously mentioned, only one-third of the geometry was modeled in the simulation. Fig. 6 shows the adopted boundary conditions.

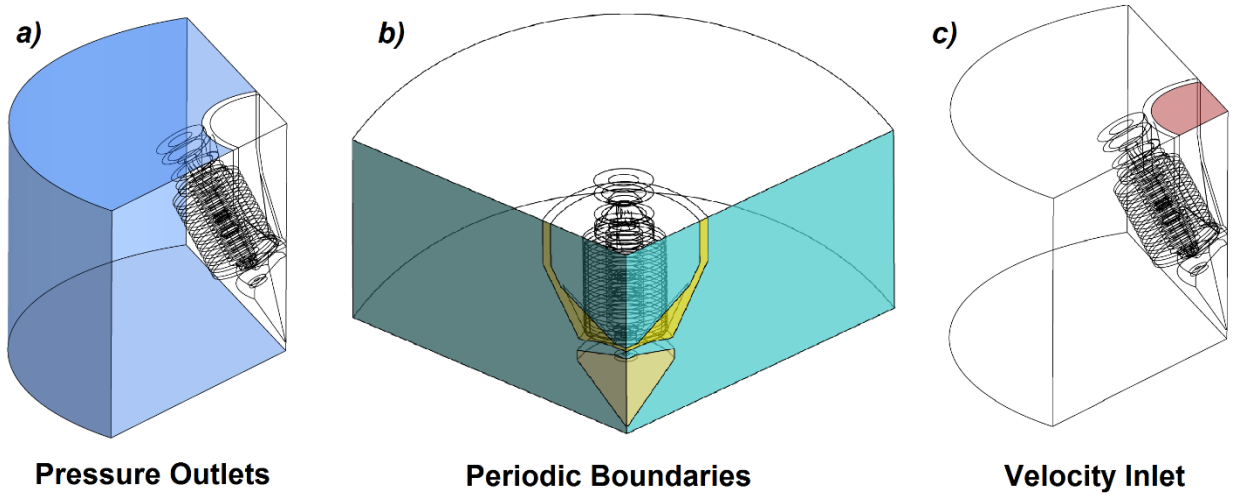

Fig. 6 Boundary conditions used for numerical simulations

The gauge pressure at the pressure outlet boundaries (Fig. 6a) was considered to be zero, as it was sufficiently far from the main flow stream. The static temperature at these boundaries was equalized with the ambient temperature $27°C$. The internal emissivity for all of these boundaries was assumed to be 1.

The no-pressure-drop periodic boundaries (Fig. 6b) used in this study implies that velocity components repeat themselves as follows:

$$u_r(r,\theta,z) = u_r\left(r,\theta+\frac{2\pi}{3},z\right) = u_r\left(r,\theta+\frac{4\pi}{3},z\right)$$
$$u_\theta(r,\theta,z) = u_\theta\left(r,\theta+\frac{2\pi}{3},z\right) = u_\theta\left(r,\theta+\frac{4\pi}{3},z\right) \quad (7)$$
$$u_z(r,\theta,z) = u_z\left(r,\theta+\frac{2\pi}{3},z\right) = u_z\left(r,\theta+\frac{4\pi}{3},z\right)$$

The same applies to the temperature.

$$T(r,\theta,z) = T\left(r,\theta+\frac{2\pi}{3},z\right) = T\left(r,\theta+\frac{4\pi}{3},z\right) \quad (8)$$

The fan airflow was modeled by velocity inlet boundary condition (Fig. 6c).

As the nozzle temperature is continuously controlled at the desired temperature by the thermistor within the feedback loop, the constant temperature of $210°C$ for PLA and $260°C$ for ABS was considered for the Diamond nozzle domain.

In conjugate boundaries, equality of the temperature and heat flux for corresponding cells on the boundaries were provided.

3.3. Mesh study

A mesh convergence study was performed to ensure that obtained results are independent of mesh discretization. 4 different mesh sizes were tested and brought in Table 2. Mesh 2, shown in Fig. 7, was used throughout the study as it provided a good compromise between accuracy and computational costs. Increased mesh resolution produced negligible

changes in the temperature values (the variable of interest), while in lower resolution (Mesh 3), slight inaccuracies were observed.

Table 2 The number of elements in the four different meshes used in this study

Mesh number	Number of elements
Mesh 1	2,943,883
Mesh 2	1,792,806
Mesh 3	853,729
Mesh 4	456,380

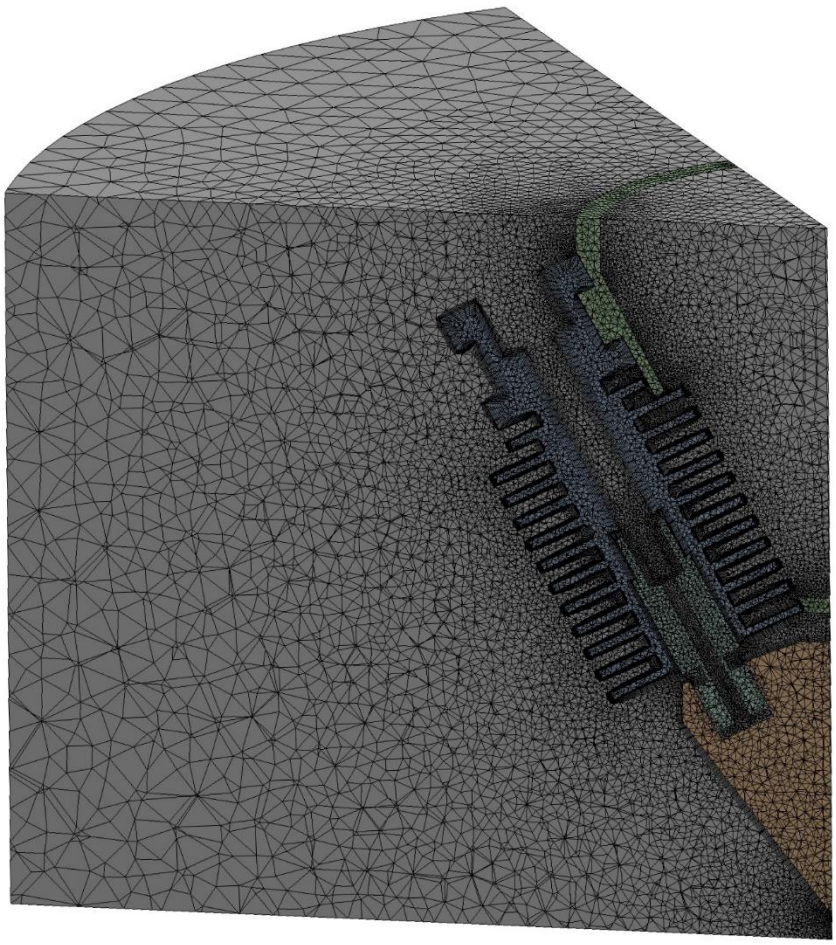

Fig. 7 A section of the selected mesh for this study

4. Results and Discussion

To study the thermal conditions leading to clogging, comprehensive knowledge about temperature changes in the hot-end is essential. Although experiments can give us reliable results about the temperature distribution along the heat sink, they cannot give a detailed picture of the temperature distribution in the heat barrier and near the nozzle. Therefore, the necessity of numerical simulation becomes more evident. In the following, the heatsink temperature distribution obtained from numerical simulations is first compared with the experimental results at zero and then at non-zero fan airflow velocities to check their agreement. The contribution of radiation heat transfer is also investigated in both cases. Then, the clogging mechanism is investigated, for which the results of the validated numerical model are compared and combined with the experiment results.

4.1 The hot-end thermal analysis

4-1-1 Heat sink thermal analysis at zero airflow velocity

Although the amount of voltage applied to the fan was known in each of the experiments, the value of the fan airflow velocity resulting from the applied voltage was not known except when the fan was off and the fan airflow velocity was zero. Therefore, the zero-velocity condition is of high importance to evaluate the numerical simulation. However, it seems this condition has not been considered earlier with the justification that turning off the fan is not recommended in the actual printing process [18].

The study of the zero-airflow condition illustrates the significance of considering radiation heat transfer. Four different nozzle temperatures of $100^{\circ}C$, $125^{\circ}C$, $150^{\circ}C$, and $200^{\circ}C$ were considered for investigating the zero-airflow velocity condition to validate our numerical simulation.

Fig. 8 shows the comparison of the heat sink temperature distribution resulted from numerical simulations, with experimental measurements in the zero-velocity condition at four different nozzle temperatures. As the figure shows, there is a good agreement between the numerical results and the experimental measurements when the radiation model is included. But neglecting the radiation heat transfer in numerical simulations adversely affects the results to the extent that it causes an error of up to $17^{\circ}C$ at the nozzle temperature of $200^{\circ}C$. However, it is expected that at higher fan airflow velocities, this error will be reduced (this will be discussed below).

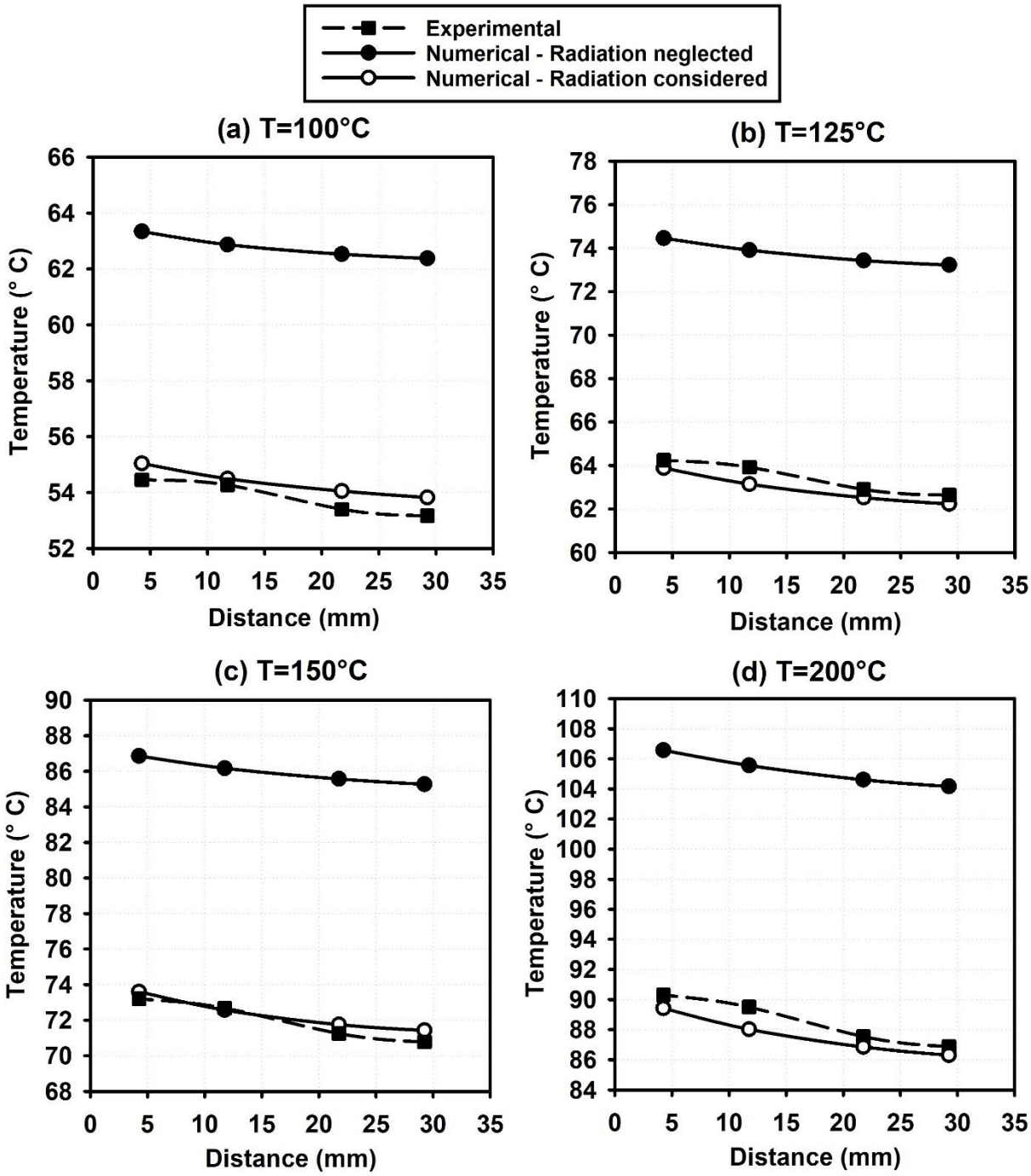

Fig. 8 Comparing experimental temperature values along the heat sink with the temperature values obtained from the numerical simulation at zero airflow velocity condition (when the fan is turned off) at four nozzle temperatures of $100^{\circ}C$, $125^{\circ}C$, $150^{\circ}C$ and $200^{\circ}C$

4-1-2 Heat sink thermal analysis at non-zero airflow velocities

For the experimental investigation of non-zero velocity conditions, different airflow rates were created by applying different voltages to the cooling fan. Then, by comparing the experimental results of heat sink temperature distribution with numerical results, the cooling airflow velocity was obtained for each of the applied voltages according to Table 3.

Table 3 Equivalent airflow velocity of each fan applied voltage

Percentage of input voltage to the board applied to the fan	15%	20%	30%	40%	50%	60%
The voltage applied to the fan (V)	1.8	2.4	3.6	4.8	6	7.2
Equivalent velocity obtained from simulation (m/s)	0.048	0.112	0.289	0.445	0.571	0.649

Finding equivalent velocities is essential because presenting the results in terms of fan voltages is useless unless the cooling fan is exactly similar to the one used in this study.

Fig. 9 illustrates the temperature distribution along the heat sink obtained from experimental measurements and numerical simulations for PLA and ABS printing processes (nozzle temperatures of $210^{\circ}C$ and $260^{\circ}C$ respectively). Aside from good agreement observed between numerical and experimental results, Fig. 9 demonstrates that by increasing the fan airflow velocity, we reach a point that further increase in air velocity does not cause much change in the heat sink temperature distribution. This is the main reason why further voltage percentages were not studied.

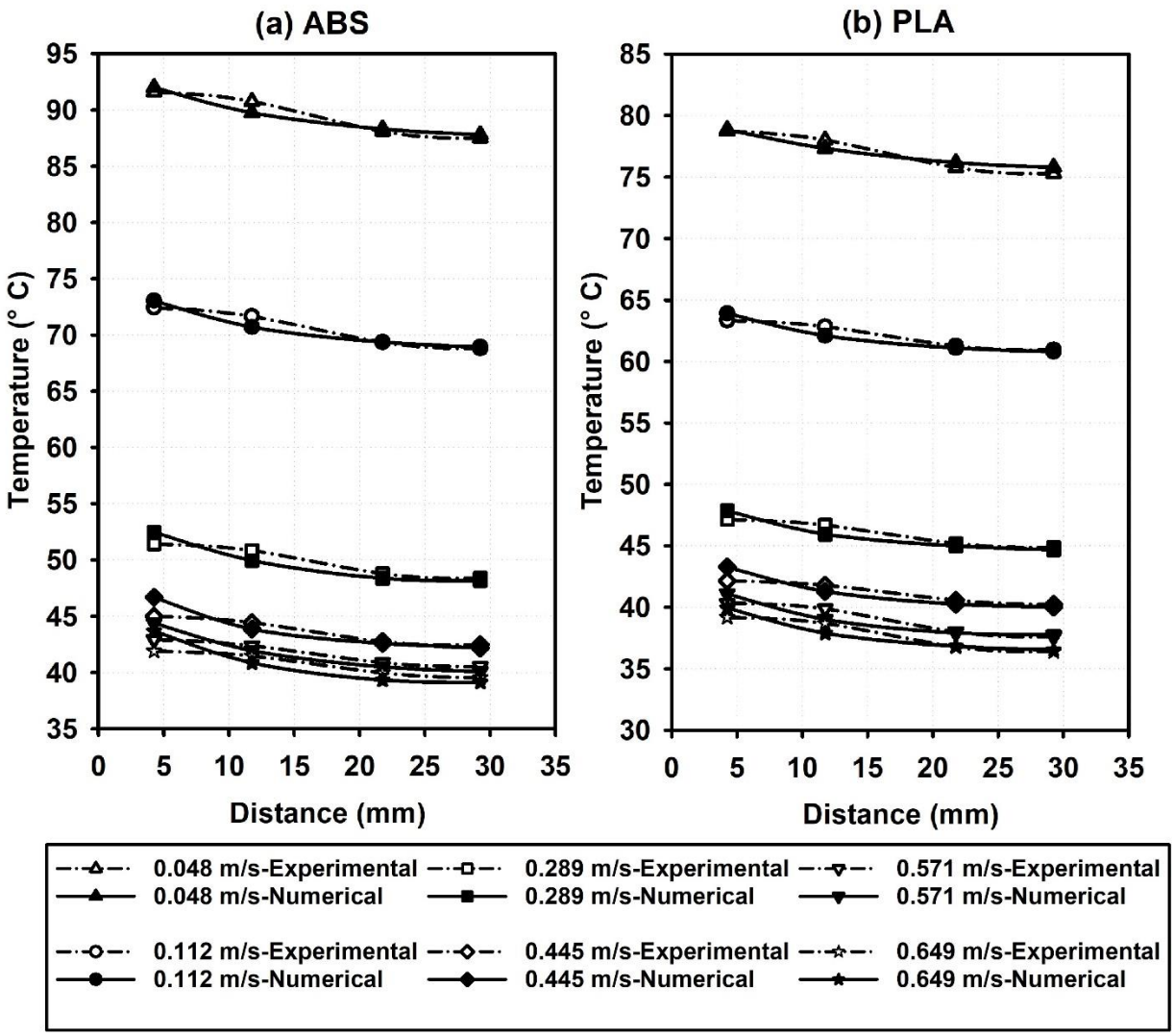

Fig. 9 Temperature distribution along the heat sink resulted from the numerical simulations compared with experimental results for ABS and PLA printing processes

Fig. 10 shows the air velocity vectors around the hot-end at two different fan airflow velocities of $0.048 m/s$ and $0.571 m/s$. At the airflow velocity of $0.048 m/s$ the contribution of forced convection in heat transfer is negligible, and the heat sink temperature is high compared to the surrounding temperature. Therefore, the convection and radiation heat transfer rates are comparable. According to Fig. 10(b), increasing the airflow velocity to $0.571 m/s$ and enhancing forced convection heat transfer causes a significant reduction in the heat sink temperature and its difference with the

surrounding temperature. So, the effect of radiation heat transfer is expected to be negligible at higher airflow velocities.

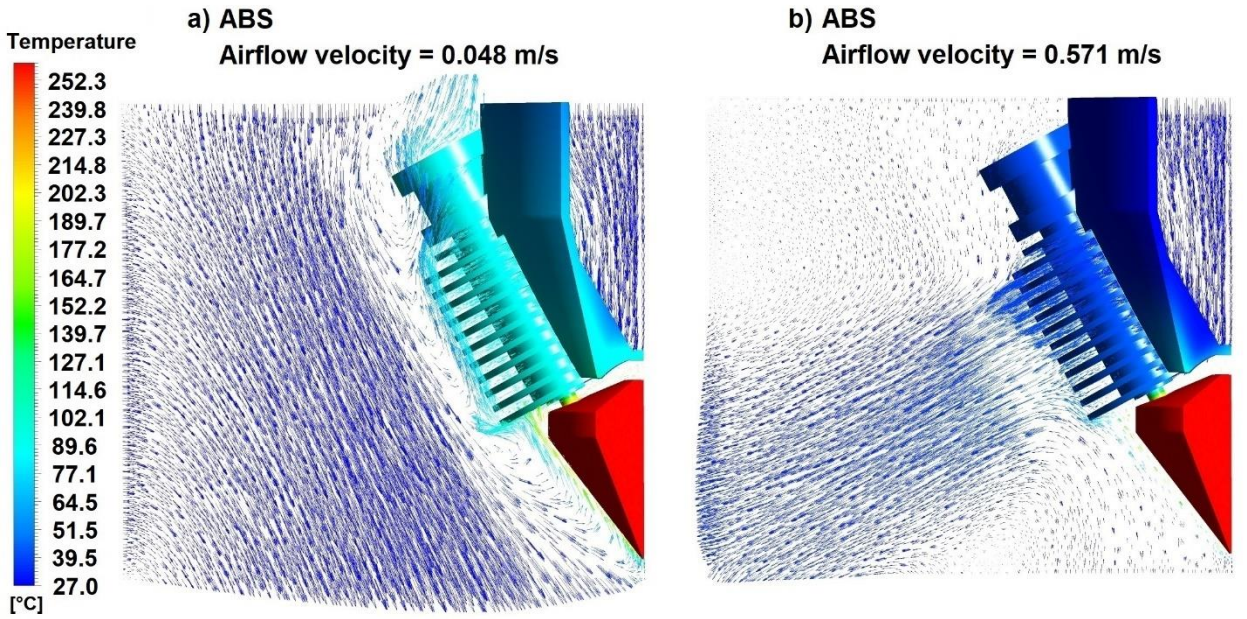

Fig. 10 Airflow velocity vectors over the Diamond hot-end during ABS 3D printing process with cooling airflow velocity of 0.048m/s and 0.571m/s

In order to determine precisely when the radiation heat transfer can be ignored, the effect of considering radiation heat transfer in numerical simulations at different fan airflow velocities was investigated for both PLA and ABS printing processes. As Fig. 11 shows, for air velocities of $0.2m/s$ and greater, radiation heat transfer can be safely neglected with no considerable effect on the heat sink temperature distribution.

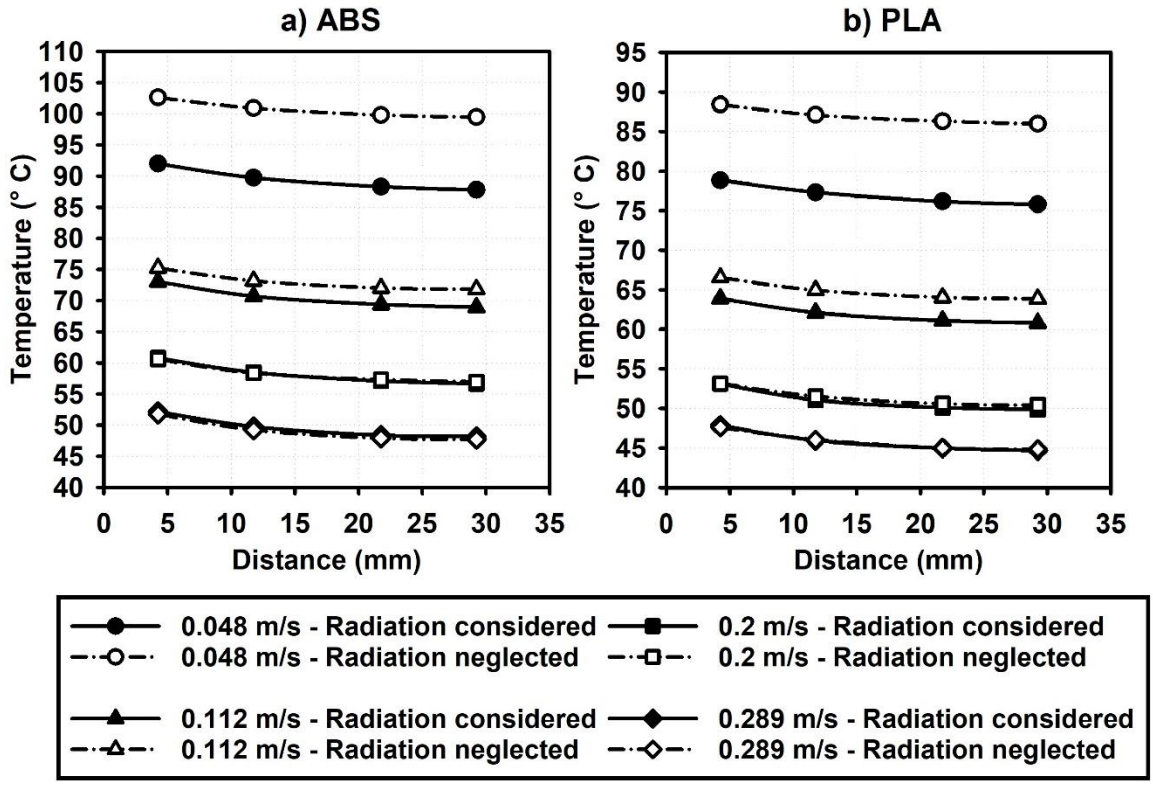

Fig. 11 The effect of radiative heat transfer simulation on the heat sink temperature distribution at four different airflow velocities for ABS and PLA printing processes

4-1-3 Correlation of fan air velocity and heatsink temperature

As presented in Table 3, based on the numerical simulations that proved to have a very good agreement with the experimental results, fan air velocities were determined. In order to present a correlation to predict the heat sink temperature based on the fan airflow velocity, thermistor 4, shown in Fig. 4, was selected as it was easier to measure in practical conditions.

Correlations (9) and (10) express the heat sink temperature at thermistor 4 in terms of fan airflow velocity for ABS and PLA printing processes, respectively.

$$T_{4,ABS} = 63.2\ exp(-8.74V) + 46.5\ exp(-0.26V) \quad (9)$$

$$T_{4,PLA} = 45.5\ exp(-9.53V) + 47.4\ exp(-0.41V) \quad (10)$$

In which, V is the fan airflow velocity in m/s.

Fig. 12 shows the correlations (9), (10), and experimental measurements obtained from thermistor 4. As the figure shows, the derived correlations have high accuracy in predicting the heat sink temperature at all fan airflow velocities. Considering the precision of the correlations, they can be used to determine the unknown fan airflow velocity by measuring the temperature at the specified point. Also, fig. 12 can be used to intraplate the fan airflow velocity with acceptable accuracy when the nozzle temperature is in the range of $210℃$ to $260℃$. Moreover, the result obtained in Fig. 9 is again evident here that increasing the fan airflow velocity will not always decrease the heat sink temperature significantly, and for fan velocities greater than $0.45\mathrm{m/s}$, it only increases energy consumption.

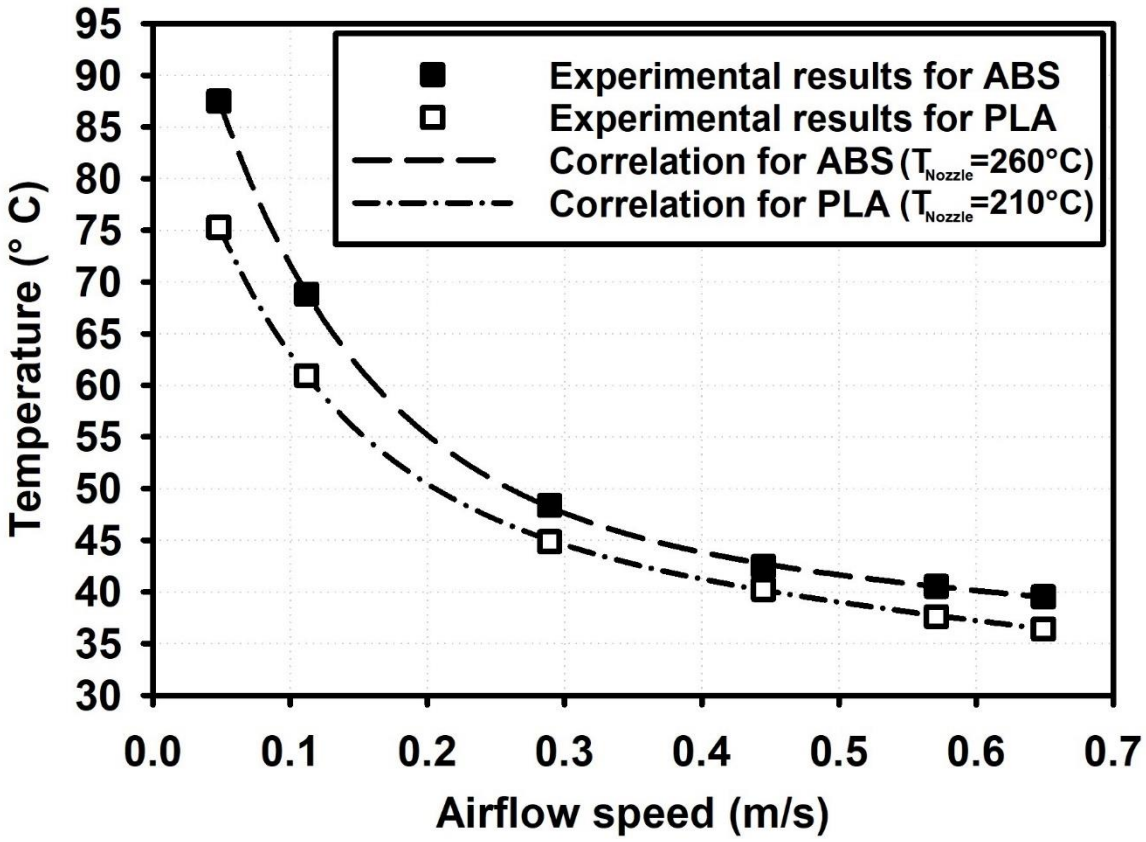

Fig. 12 Experimental results of the heat sink temperature at Thermistor 4 and derived correlations from them in terms of the fan airflow velocity for ABS and PLA

4.2. Clogging detection and prevention

In order to use the hot-end reliably and efficiently, it is important to determine the minimum airflow velocity needed to prevent clogging. As described in section 2, a series of experiments were performed to investigate the clogging problem. The experiments led to one of the following three conditions:

1. Complete clogging: in such cases, the heat barrier was completely blocked, as shown in Fig. 13(a). In this condition, unclogging the hot-end was only possible by stopping the printing process and cleaning the nozzle and heat barrier. The process had to be re-started from the beginning. The "×" mark indicates this condition in Tables 4 and 5.

2. No complete clogging, but with some problems: in this case, the filament could not be fed because a part of the filament inside the heat barrier was swelled due to high temperature and stuck to the inside wall of the heat barrier (Fig. 13(b)). Unlike the complete clogging condition, there was no need to stop the entire printing process. Instead, the process had to be paused to pull out the filament and cut off the swollen part. The "∗" mark represents this condition in Tables 4 and 5.

3. The printing process without any problem: The "✓" mark indicates this condition in Tables 4 and 5.

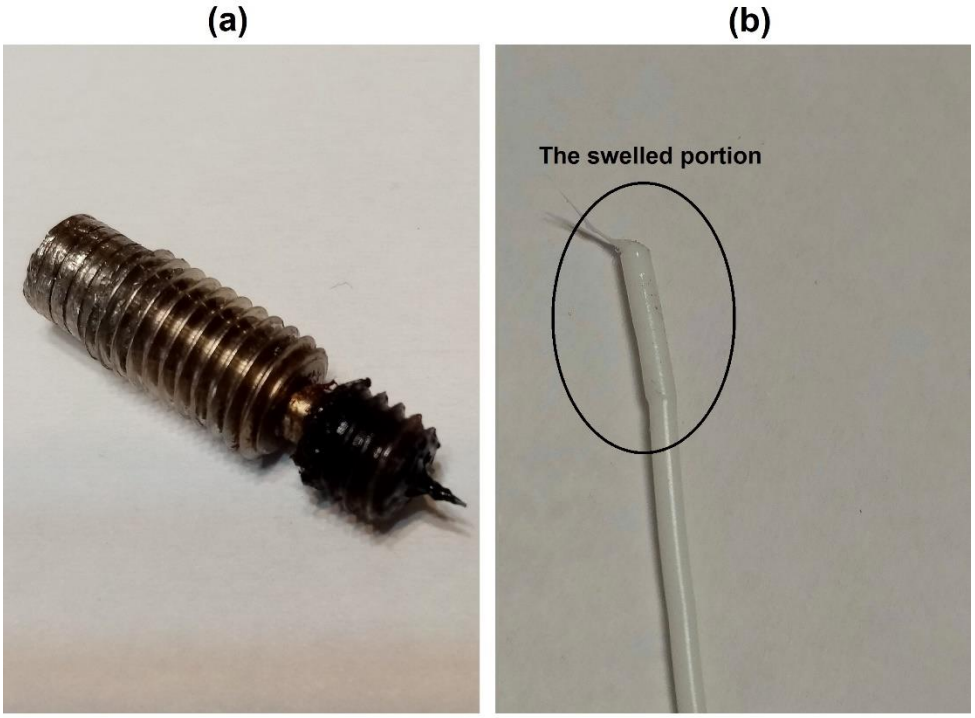

Fig. 13 (a) The completely blocked heat barrier by a black ABS filament. A case of complete clogging. (b) The swelled part of a white PLA filament due to overheating of the heat barrier

As Table 4 shows, for the PLA printing process, the complete clogging occurred when the fan air velocity was $0.112 m/s$. Table 4 also shows that the second scenario mentioned above occurred in two experiments at $0.289 m/s$. So, the airflow velocity of $0.445 m/s$ is considered the lowest possible airflow velocity that can be used reliably in this study. At this fan airflow velocity, according to correlation (10), the temperature at thermistor 4 is about $40^{\circ}C$ that can be considered as a criterion under practical conditions.

Table 4 Clogging experiment results for PLA. Each specified condition repeated four times

Fan airflow velocity(m/s)	0.571	0.445	0.289	0.112
Temperature at thermistor #4 (℃)	37.7	40.1	45.0	60.9
Test Number 1	✓	✓	✓	×

Test Number 2	✓	✓	✓	×
Test Number 3	✓	✓	∗	×
Test Number 4	✓	✓	∗	×

As can be seen in Table 5, in the ABS printing process, the clogging only happened when the fan airflow velocity was decreased to $0.048m/s$. Therefore, to avoid clogging, the airflow velocity of $0.112m/s$ seems sufficient. In this case, according to correlation (9), the temperature at thermistor 4 is about $69^{\circ}C$ that can be used as a criterion under practical conditions. It should be noted that under this condition, as shown in Fig. 9, the temperature distribution along the heat sink is in the range of $69°C$ to $73°C$ that is higher than the T_g of PLA. Therefore, if the Diamond hot-end cooler shield is made of PLA or other materials with similar T_g, higher airflow velocities should be considered to prevent thermal damages.

Table 5 Clogging experiment results for ABS. Each specified condition repeated four times

Fan airflow velocity (m/s)	0.445	0.289	0.112	0.048
Temperature at thermistor #4 (℃)	42.7	48.2	68.9	87.5
Test Number 1	✓	✓	✓	×
Test Number 2	✓	✓	✓	×
Test Number 3	✓	✓	✓	×
Test Number 4	✓	✓	✓	×

4-3 Clogging mechanism

In material extrusion additive manufacturing, the pressure required to extrude the molten material is provided by the solid filament above it. In fact, the unmelted filament acts as a piston and pushes the molten filament

through the nozzle. But based on the results of this research, insufficient hot-end cooling condition and heat barrier overheating cause the temperature of a significant length of the filament within the heat barrier to rise above the filament glass transition temperature (T_g). Therefore, under the stepper motor's driving force, it cannot play its role and, instead, it deforms. Fig. 14 shows the part of the filament pulled out of the heat barrier after the clogging occurred, and it well illustrates the condition described.

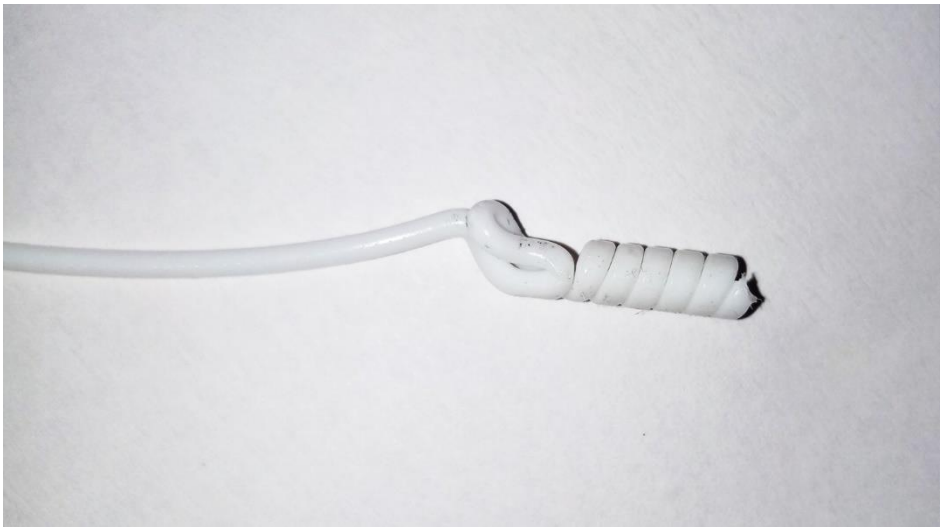

Fig. 14 The PLA filament inside the heat barrier is heated up to the glass transition temperature due to insufficient cooling and is twisted under the driving force of the stepper motor

Fig. 15 shows the temperature distribution of the heat sink and the filament inside the heat barrier for the ABS and PLA printing processes at three different airflow velocities. According to Fig. 15, as airflow velocity decreases, the temperature gradient declines. Accordingly, the length of the filament, which is at a temperature higher than the glass transition temperature, ℓ, increases so that it eventually buckles under the extruder motor force.

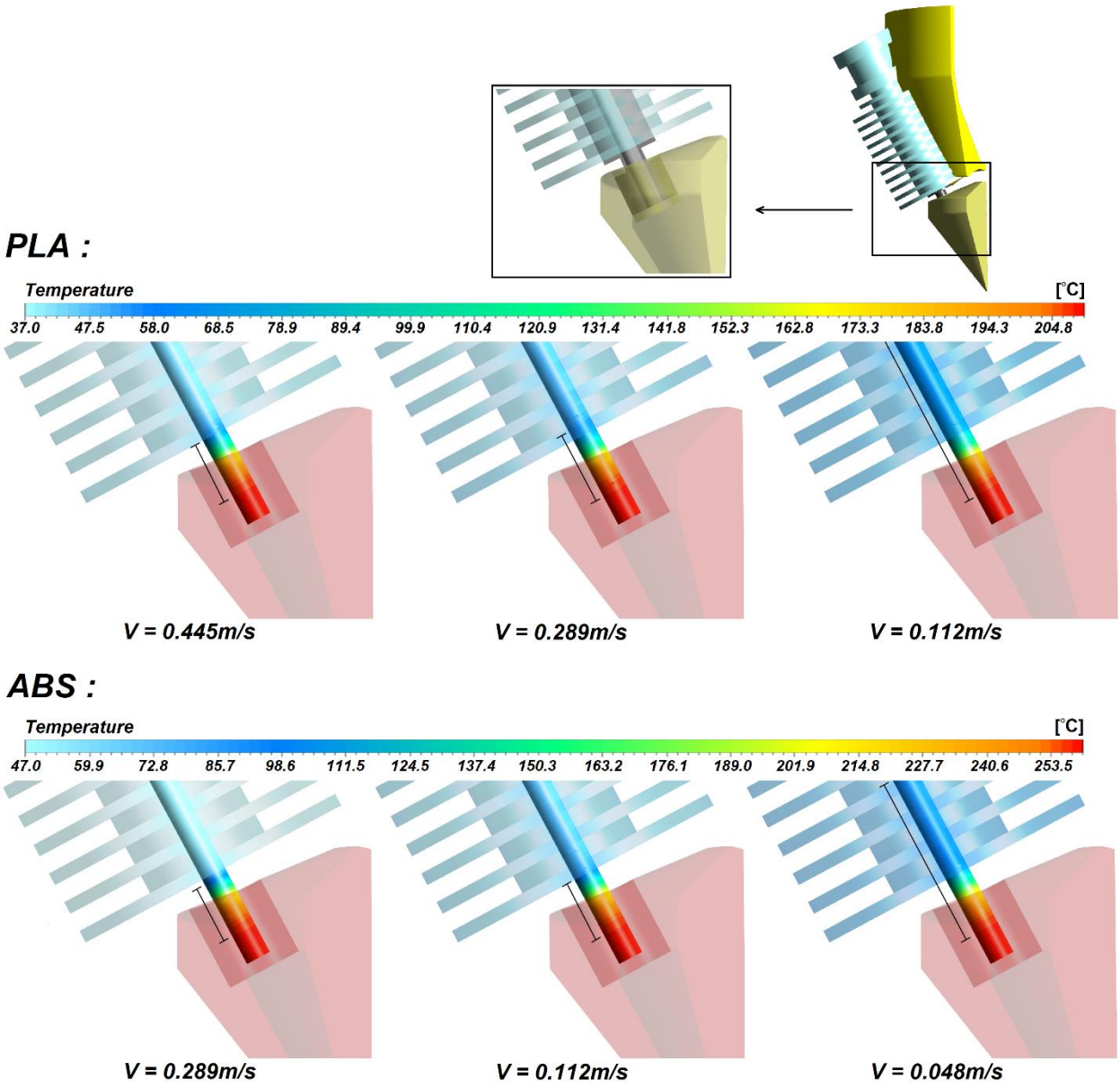

Fig.15 The temperature contour of the filament inside the heat barrier at three different fan airflow velocities. In the clogging cases, the length ℓ increases considerably

The force applied by the extruder motor to the filament, F_m can be determined by knowing the pressure drop in the nozzle, ΔP.

$$F_m = \Delta P \times A_f \quad (11)$$

In which, A_f is filament cross-section area. The pressure drop in a tube with length l and radius r is given by [29,30]:

$$\Delta P = \frac{8\mu Q l}{\pi r^4} \quad (12)$$

In which μ is the viscosity at nozzle temperature which is approximately $100\ Pa.s$ for PLA [31] and $350\ Pa.s$ for ABS [32] assuming that the shear rate in the nozzle is about $575 s^{-1}$ [33] and Q is the flow rate and can be roughly calculated as follow:

$$Q = H_l \times W_l \times V_p \quad (13)$$

In which H_l is layer height, W_l is layer width, and V_p is print velocity. This pressure is applied through the solid part to the melted material. On the other hand, the critical buckling load for elastic columns is given by [34]:

$$F_{buckling} = \frac{\pi^2 EI}{(L_e)^2} \quad (14)$$

In which, E is the elastic modulus of the material, I is the second moment of area, L_e is the column effective length which in the case of both ends pinned, the value would be $L_e = \ell$. The critical length can be calculated from Eq. 11 and Eq. 14:

$$L_{crt} = \sqrt{\frac{\pi^2 E R^2}{4(\Delta P)}} \quad (15)$$

In which R is the filament radius.

It should be noted that Eq. 15 can only give a rough approximation of the critical length (L_{crt}) mainly because it assumes the behavior of the material to be quite elastic. Also, the module values for both PLA and ABS were considered constant at the average temperature of that region and obtained from the literature [35,36].

However, the calculated L_{crt} still shows a relatively good match with the experimental and numerical simulation results.

Fig. 16 illustrates the length ℓ resulted from numerical simulations at different fan airflow velocities for the ABS printing process. As the figure shows, by

decreasing the fan airflow velocity to around $0.048m/s$, the length ℓ increases so that it exceeds the critical length calculated from Eq. 15, and eventually, it buckles and clogs the hot-end. This is entirely in agreement with the experimental results presented in Table (5).

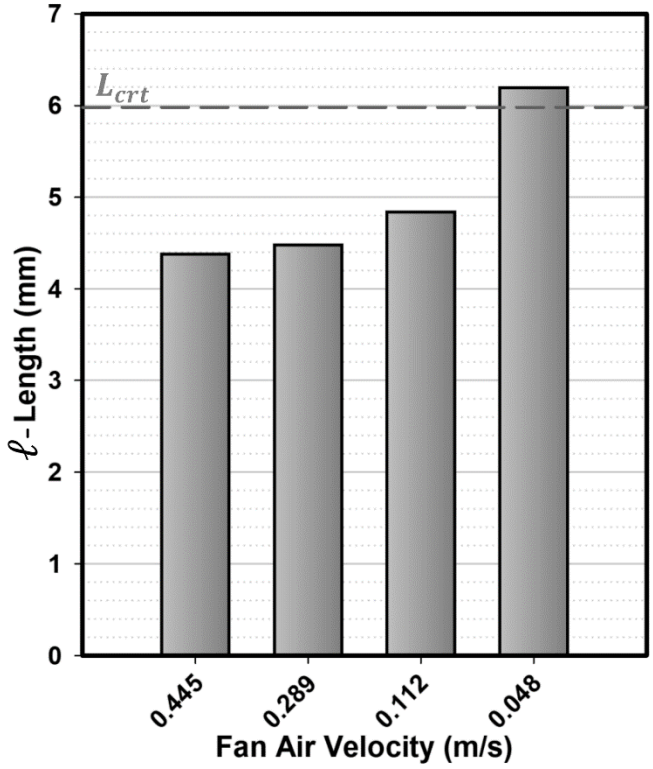

Fig.16 The length of the filament, which is at a temperature higher than glass transition temperature, ℓ, at different fan airflow velocities during ABS printing process

A similar analysis can be applied to the PLA printing process. Fig. 17 shows the length ℓ resulted from numerical simulations at different fan airflow velocities for the PLA printing process. Similarly, when the length ℓ exceeds the critical length (L_{crt}), the clogging happens, which is in agreement with the experimental results presented in Table (4). Interestingly, Fig. 17 suggests that the second scenario that happened in airflow speed of $0.289m/s$ in the PLA printing process can be explained by the closeness of the length ℓ and L_{crt}.

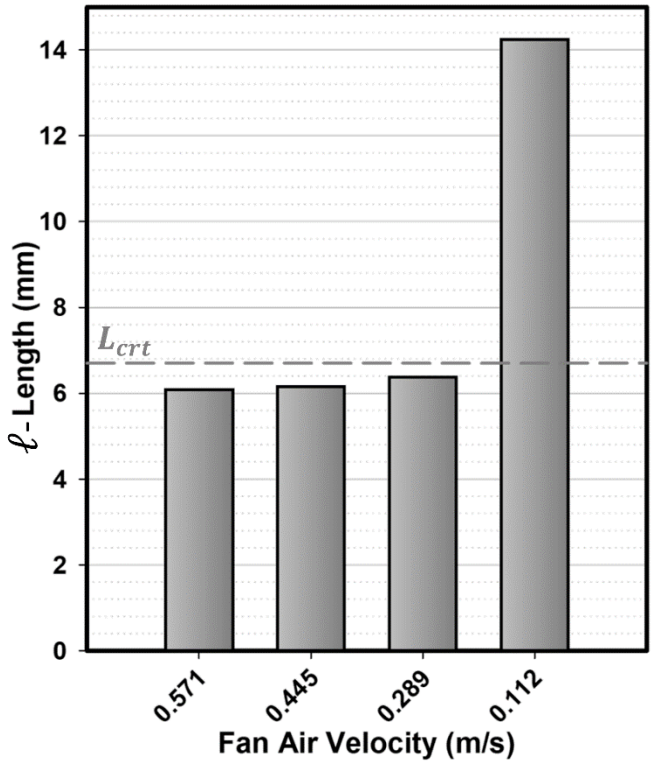

Fig.17 The length of the filament, which is at a temperature higher than glass transition temperature, ℓ, at different fan airflow velocities during PLA printing process

The analogous thermal behavior of two different thermoplastics of PLA and ABS in terms of clogging suggests that when the length ℓ exceeds the critical length (L_{crt}), the filament buckles in this region. This is the main reason for clogging in filament-based material extrusion printing process of thermoplastics. Our rough estimate of the critical length (L_{crt}) in both ABS and PLA printing processes matches very well with the experimental observations and numerical results, although more research can be done in this area to determine more precise value of L_{crt}.

Moreover, since the geometry of the heat sink and the heat barrier in the Diamond hot-end are similar to those in E3D hot-ends, the same analysis about clogging occurrence can be applied to them. Also, the practical criteria of $40°C$ and $69°C$ presented for T_4 to prevent clogging in the printing process

of PLA and ABS, respectively, still gives a good approximation for E3D hot-ends. However, the input airflow velocities corresponding to those temperatures may differ.

5. Conclusion

Thermal performance and the potential conditions leading to clogging inside a hot-end were studied experimentally and numerically. A core x-y filament-based material extrusion 3D printer constructed by authors was equipped with a RepRap multi-material Diamond hot-end. The heat sink temperature was measured in a wide range of airflow rates at the nozzle temperatures of $210℃$ and $260℃$ (for PLA and ABS, respectively). Also, to find a criterion for predicting the clogging occurrence, a series of experiments were performed by printing a cube of $15mm \times 15mm \times 20mm$ dimensions and under different airflow velocities for both PLA and ABS printing processes.

Moreover, a 3D finite volume model of the Diamond hot-end was developed to analyze the hot-end thermal behavior during the printing process. The numerical simulation results were in good agreement with experimental data in the whole air velocity range, including the zero-velocity condition, which was the only pre-known velocity condition in the experiments, so it was highly important in evaluating the numerical simulation. The derived conclusions of this study can be summarized as follows:

- Numerical simulation of the Diamond hot-end agreed well with experimental results. The study of the effects of radiation heat transfer showed that for air velocities of $0.2m/s$ and greater, radiation heat transfer could be safely neglected as it had no considerable effect on the heat sink temperature distribution. But in lower cooling airflow velocities, this heat transfer mechanism cannot be ignored.

- Mathematical correlations for predicting the heat sink temperature were presented. For both PLA and ABS printing processes, the temperature at a certain point in the upper part of the sink (location of thermistor 4, as a convenient place for practical measurements) was presented in terms of cooling airflow velocity.
- In both PLA and ABS printing processes, as the airflow velocity increases, the heat sink temperature decreases steadily. But for velocities more than $0.45 m/s$, while the power demand increases, no significant change in the sink temperature was observed.
- To avoid clogging in the Diamond hot-end, the maximum heat sink temperature in its upper part (thermistor 4) should be less than $40°C$ for PLA (equivalent to the fan airflow velocity of $0.445 m/s$ or more) and less than $69°C$ for ABS printing process (equivalent to the fan airflow velocity of $0.112 m/s$ or more). Due to geometrical similarities, these temperature criteria can also be considered as a good approximation for other similar hot-ends like E3d hot-ends.
- Experimental and numerical studies on both PLA and ABS printing processes revealed that the clogging problem depends on the length of the filament, whose temperature is higher than the glass transition temperature. When this length exceeds the critical length, the filament buckles, and clogging occurs. This conclusion may be generalized to other thermoplastics, while more investigations are needed to confirm it.

Declaration

Funding

The authors declare they have no financial interests.

Conflicts of interest

The authors have no conflicts of interest to declare that are relevant to the content of this article.

Availability of data and materials

All data generated or analysed during this study are included in this published article and its supplementary information files.

Consent to publish

Not applicable.

Consent to participate

Not applicable.

Ethical approval

Not applicable.

Author's contributions

Z. Taheri and A. Karimnejad Esfahani conceived of the presented idea. Z.Taheri carried out the experiments. Z. Taheri and A. Karimnejad Esfahani designed the model and the computational framework and analysed the data. A. Ramiar encouraged Z. Taheri and A. Karimnejad Esfahani to investigate clogging phenomenon and supervised the findings of this work. All authors discussed the results and contributed to the final manuscript.

References

1. 3D Printing Market by Offering (Printer, Material, Software, Service), Process (Binder Jetting, Direct Energy Deposition, Material Extrusion, Material Jetting, Powder Bed Fusion), Application, Vertical, Technology, and Geography - Global Forecast to 2024. MarketsandMarkets™ INC. https://www.marketsandmarkets.com/Market-Reports/3d-printing-market-1276.html. Accessed 2020-06-28

2. Jiang J, Xu X, Stringer J (2018) Support Structures for Additive Manufacturing: A Review. Journal of Manufacturing and Materials Processing 2 (4):64. https://doi.org/10.3390/jmmp2040064

3. Yan X, Gu P (1996) A review of rapid prototyping technologies and systems. Computer-Aided Design 28 (4):307-316. https://doi.org/10.1016/0010-4485(95)00035-6

4. Balletti C, Ballarin M, Guerra F (2017) 3D printing: State of the art and future perspectives. Journal of Cultural Heritage 26:172-182. https://doi.org/10.1016/j.culher.2017.02.010

5. Short DB (2015) Use of 3D Printing by Museums: Educational Exhibits, Artifact Education, and Artifact Restoration. 3D Printing and Additive Manufacturing 2 (4):209-215. https://doi.org/10.1089/3dp.2015.0030

6. Gibson I, Cheung LK, Chow SP, Cheung WL, Beh SL, Savalani M, Lee SH (2006) The use of rapid prototyping to assist medical applications. Rapid Prototyping Journal 12 (1):53-58. https://doi.org/10.1108/13552540610637273

7. Culmone C, Smit G, Breedveld P (2019) Additive manufacturing of medical instruments: A state-of-the-art review. Additive Manufacturing 27:461-473. https://doi.org/10.1016/j.addma.2019.03.015

8. Zhou X, Feng Y, Zhang J, Shi Y, Wang L (2020) Recent advances in additive manufacturing technology for bone tissue engineering scaffolds. The International Journal of Advanced Manufacturing Technology 108 (11-12):3591-3606. https://doi.org/10.1007/s00170-020-05444-1

9. McCaw JCS, Cuan-Urquizo E (2020) Mechanical characterization of 3D printed, non-planar lattice structures under quasi-static cyclic loading. Rapid Prototyping Journal 26 (4):707-717. https://doi.org/10.1108/RPJ-06-2019-0163

10. Straub J (2015) Initial Work on the Characterization of Additive Manufacturing (3D Printing) Using Software Image Analysis. Machines 3 (2):55-71. https://doi.org/10.3390/machines3020055
11. Straub J (2016) Characterization of internal geometry / covered surface defects with a visible light sensing system. Paper presented at the Image Sensing Technologies: Materials, Devices, Systems, and Applications III, International Society for Optics and Photonicshttps. https://doi.org/10.1117/12.2227802
12. Ceruti A, Liverani A, Bombardi T (2017) Augmented vision and interactive monitoring in 3D printing process. International Journal on Interactive Design and Manufacturing (IJIDeM) 11 (2):385-395. https://doi.org/10.1007/s12008-016-0347-y
13. Tlegenov Y, Hong GS, Lu WF (2018) Nozzle condition monitoring in 3D printing. Robotics and Computer-Integrated Manufacturing 54:45-55. https://doi.org/10.1016/j.rcim.2018.05.010
14. Bukkapatnam S, Clark B (2007) Dynamic Modeling and Monitoring of Contour Crafting—An Extrusion-Based Layered Manufacturing Process. Journal of Manufacturing Science and Engineering 129 (1):135-142. https://doi.org/10.1115/1.2375137
15. Ivanova O, Williams C, Campbell T (2013) Additive manufacturing (AM) and nanotechnology: promises and challenges. Rapid Prototyping Journal 19 (5):353-364. https://doi.org/10.1108/RPJ-12-2011-0127
16. Beran T, Mulholland T, Henning F, Rudolph N, Osswald TA (2018) Nozzle clogging factors during fused filament fabrication of spherical particle filled polymers. Additive Manufacturing 23:206-214. https://doi.org/10.1016/j.addma.2018.08.009
17. E3D-ONLINE V6 Troubleshooting - E3D-Online. https://e3d

online.dozuki.com/Wiki/V6_Troubleshooting. Accessed 2020-06-28
18. Jerez-Mesa R, Travieso-Rodriguez JA, Corbella X, Busqué R, Gomez-Gras G (2016) Finite element analysis of the thermal behavior of a RepRap 3D printer liquefier. Mechatronics 36:119-126. https://doi.org/10.1016/j.mechatronics.2016.04.007
19. Jerez-Mesa R, Gomez-Gras G, Travieso-Rodriguez JA, Garcia-Plana V (2018) A comparative study of the thermal behavior of three different 3D printer liquefiers. Mechatronics 56:297-305. https://doi.org/10.1016/j.mechatronics.2017.06.008
20. Hertafeld E, Zhang C, Jin Z, Jakub A, Russell K, Lakehal Y, Andreyeva K, Bangalore SN, Mezquita J, Blutinger J, Lipson H (2019) Multi-Material Three-Dimensional Food Printing with Simultaneous Infrared Cooking. 3D Printing and Additive Manufacturing 6 (1):13-19. https://doi.org/10.1089/3dp.2018.0042
21. Hosny A, Keating SJ, Dilley JD, Ripley B, Kelil T, Pieper S, Kolb D, Bader C, Pobloth A-M, Griffin M, Nezafat R, Duda G, Chiocca EA, Stone JR, Michaelson JS, Dean MN, Oxman N, Weaver JC (2018) From Improved Diagnostics to Presurgical Planning: High-Resolution Functionally Graded Multimaterial 3D Printing of Biomedical Tomographic Data Sets. 3D Printing and Additive Manufacturing 5 (2):103-113. https://doi.org/10.1089/3dp.2017.0140
22. Mirzaali MJ, Caracciolo A, Pahlavani H, Janbaz S, Vergani L, Zadpoor AA (2018) Multi-material 3D printed mechanical metamaterials: Rational design of elastic properties through spatial distribution of hard and soft phases. Applied Physics Letters 113 (24):241903. https://doi.org/10.1063/1.5064864
23. Song H, Martínez J, Bedell P, Vennin N, Lefebvre S (2019) Colored

Fused Filament Fabrication. ACM Transactions on Graphics 38 (5):1-11. doi:10.1145/3183793

24. Baca D, Ahmad R (2020) The impact on the mechanical properties of multi-material polymers fabricated with a single mixing nozzle and multi-nozzle systems via fused deposition modeling. The International Journal of Advanced Manufacturing Technology 106 (9):4509-4520. https://doi.org/10.1007/s00170-020-04937-3

25. Slic3r Manual – Cooling. https://manual.slic3r.org/expert-mode/cooling. Accessed 2020-06-30

26. Slic3r Manual – Fighting Ooze. https://manual.slic3r.org/expert-mode/fighting-ooze. Accessed 2020-06-30

27. Wilcox D (1998) Turbulence Modeling for CFD, vol 2. DCW industries, La Canada, California

28. Launder BE, Spalding DB (1972) Lectures in mathematical models of turbulence. London, New York, Academic Press

29. Van Wazer JR (1963) Viscosity and flow measurement: a laboratory handbook of rheology. Interscience Publishers.

30. Barnes HA, Hutton JF, Walters K (1989) An introduction to rheology, vol 3. Elsevier.

31. Cobos CM, Garzón L, López Martinez J, Fenollar O, Ferrandiz S (2019) Study of thermal and rheological properties of PLA loaded with carbon and halloysite nanotubes for additive manufacturing. Rapid Prototyping Journal 25 (4):738-743. https://doi.org/10.1108/RPJ-11-2018-0289

32. Heller BP, Smith DE, Jack DA (2016) Effects of extrudate swell and nozzle geometry on fiber orientation in Fused Filament Fabrication nozzle flow. Additive Manufacturing 12:252-264.

https://doi.org/10.1016/j.addma.2016.06.005
33. Heller BP, Smith DE, Jack DA (2015) Effect of Extrudate Swell, Nozzle Shape, and Convergence Zone on Fiber Orientation in Fused Deposition Modeling Nozzle Flow. Proceedings of the Solid Freeform Fabrication, Austin, TX, USA:1220-1236.
34. Popov E, Balan T, Engineering mechanics of solids, 1999. Prentice-Hall.
35. Yousefzade O, Jeddi J, Vazirinasab E, Garmabi H (2019) Poly(lactic acid) phase transitions in the presence of nano calcium carbonate: Opposing effect of nanofiller on static and dynamic measurements. Journal of Thermoplastic Composite Materials 32 (3):312-327. https://doi.org/10.1177/0892705718759386
36. En-Naji A, Mouhib N, Lahlou M, Farid H, El Ghorba M (2019) Change of experimental young’s modulus with increasing temperature for an ABS material subjected to tensile test. ARPN Journal of Engineering and Applied Sciences 14 (3):708-717.